International Journal of Applied Earth Observation and Geoinformation 33 (2014) 243–254

Contents lists available at ScienceDirect

International Journal of Applied Earth Observation and Geoinformation

journal homepage: www.elsevier.com/locate/jag

Automatic and improved radiometric correction of Landsat imagery using reference values from MODIS surface reflectance images

X. Pons [a,*], L. Pesquer [b], J. Cristóbal [c], O. González-Guerrero [a]

[a] Grumets Research Group, Dep Geografia, Edifici B, Universitat Autònoma de Barcelona, 08193 Bellaterra, Catalonia, Spain
[b] Grumets Research Group, CREAF, Edifici C, Universitat Autònoma de Barcelona, 08193 Bellaterra, Catalonia, Spain
[c] Geophysical Institute and Institute of Northern Engineering, University of Alaska Fairbanks, 903 Koyukuk Dr, Fairbanks, USA

ARTICLE INFO

Article history:
Received 19 March 2014
Accepted 12 June 2014
Available online 29 June 2014

Keywords:
Radiometric correction
Landsat
MODIS
Pseudoinvariant area

ABSTRACT

Radiometric correction is a prerequisite for generating high-quality scientific data, making it possible to discriminate between product artefacts and real changes in Earth processes as well as accurately produce land cover maps and detect changes. This work contributes to the automatic generation of surface reflectance products for Landsat satellite series. Surface reflectances are generated by a new approach developed from a previous simplified radiometric (atmospheric + topographic) correction model. The proposed model keeps the core of the old model (incidence angles and cast-shadows through a digital elevation model [DEM], Earth–Sun distance, etc.) and adds new characteristics to enhance and automatize ground reflectance retrieval. The new model includes the following new features: (1) A fitting model based on reference values from pseudoinvariant areas that have been automatically extracted from existing reflectance products (Terra MODIS MOD09GA) that were selected also automatically by applying quality criteria that include a geostatistical pattern model. This guarantees the consistency of the internal and external series, making it unnecessary to provide extra atmospheric data for the acquisition date and time, dark objects or dense vegetation. (2) A spatial model for atmospheric optical depth that uses detailed DEM and MODTRAN simulations. (3) It is designed so that large time-series of images can be processed automatically to produce consistent Landsat surface reflectance time-series. (4) The approach can handle most images, acquired now or in the past, regardless of the processing system, with the exception of those with extremely high cloud coverage. The new methodology has been successfully applied to a series of near 300 images of the same area including MSS, TM and ETM+ imagery as well as to different formats and processing systems (LPGS and NLAPS from the USGS; CEOS from ESA) for different degrees of cloud coverage (up to 60%) and SLC-off. Reflectance products have been validated with some example applications: time series robustness (for a pixel in a pseudoinvariant area, deviations are only 1.04% on average along the series), spectral signatures generation (visually coherent with the MODIS ones, but more similar between dates), and classification (up to 4 percent points better than those obtained with the original manual method or the CDR products). In conclusion, this new approach, that could also be applied to other sensors with similar band configurations, offers a fully automatic and reasonably good procedure for the new era of long time-series of spatially detailed global remote sensing data.

Introduction

The Landsat satellite programme has been collecting imagery since 1972. It is one of the longest continuously acquired collections of Earth observation data and has the highest impact for scientific, management and policy-making purposes at detailed spatial resolution (Goward and Masek, 2001). Moreover, it is the most commonly used remotely sensed satellite imagery in Landscape Ecology studies (Newton et al., 2009) followed by NOAA-AVHRR and SPOT-HRV/HRG. In addition, in 2008 the United States Geological Survey (USGS) released the Landsat archive, thus greatly increasing its use by the scientific community (Vermote et al., 2008).

The distribution and processing level of Landsat imagery has changed since 1972, and therefore the post-processing steps, mainly geometric and radiometric correction, have also changed. In the case of the USGS, Landsat Level 1G (system correction of sensor and platform derived distortions) was the standard product

* Corresponding author. Tel.: +34 935 811 527; fax: +34 935 812 001.
E-mail address: Xavier.Pons@uab.cat (X. Pons).

http://dx.doi.org/10.1016/j.jag.2014.06.002

until 2008, when USGS started to provide a georeferenced L1T (terrain corrected) product. Landsat Surface Reflectance products have been freely available since 2013 through the Climate Data Record (CDR) (U.S. Geological Survey, 2013) generated from the Landsat Ecosystem Disturbance Adaptive Processing System (LEDAPS) based on the work by Masek et al. (2006). Although the list of existing reflectance products is continuously updated (see http://landsat.usgs.gov/documents/L4-5TM_NLAPS.xlsx), CDR product distribution from the USGS archive is currently not complete because the scenes from the National Landsat Archive Processing System (NLAPS) are not fully processed yet. Moreover, the distribution rights for scenes belonging to some regions and specific periods are assigned to other agencies, for example ESA (European Spatial Agency, 2005), resulting in a significant time lag for obtaining continuous time-series for large regions. It is worth noting that USGS considers that the applied radiometric correction is not yet consolidated, as indicated in the Product Guide "Landsat climate data record (CDR). Surface reflectance" (U.S. Geological Survey, 2013), and therefore carrying out research on Landsat radiometric correction is the next challenge.

Atmospheric conditions (water vapour, aerosols, etc.) and different illumination caused by the solar position according to the acquisition date and time, location on Earth and relief (cast shadows, etc.) may cause undesired artefacts in remote sensing images. It is therefore very important to apply the process known as radiometric correction (Pons and Solé-Sugrañes, 1994; Richards and Jia, 2005; Janzen et al., 2006). Radiometric correction is a set of techniques designed to convert the digital values captured by a sensor to physical quantities of interest, such as radiance, reflectance or surface temperature (Pons and Arcalís, 2012). This transformation is required, for example, to facilitate the comparison between the same or different remote sensors at different times, as well as to compare satellite or aerial data with data from field-based sensors (Franklin and Giles, 1995). Radiometric correction is also a prerequisite for generating high-quality scientific data (Chander et al., 2009), making it possible to discriminate between product artefacts and real changes in Earth processes (Roy et al., 2002) as well as produce accurate land cover maps and detect changes (Song et al., 2001), among other applications.

In the radiometric correction, topographic effects (mainly incidence angles and cast shadows) can be successfully taken into account using an accurate elevation source such as high resolution digital elevation models (DEM) from local cartographic institutes, or from worldwide freely available data, like the NASA Shuttle Radar Topographic Mission (Rabus et al., 2003) or the ASTER Global Digital Elevation Map (Slater et al., 2011). Although worldwide high quality DEM at medium resolution were not very available not so long ago, the current state of DEM datasets makes proper topographic correction of any optical remote sensing product possible. These datasets thus play a key role in improving radiometric correction methods (Hale and Rock, 2003; Riaño et al., 2003; Hantson and Chuvieco, 2011). To remove the atmospheric effects, detailed information on atmospheric parameters such as aerosols, water vapour and ozone is often required, being local atmospheric measurements or re-analysis data a common source of atmospheric information. However, atmospheric radiosondes are usually not available at the time of satellite pass and a single atmospheric radiosonde might not be representative of the atmospheric conditions of wide swath satellite images such as those provided by Landsat, NOAA-AVHRR and TERRA/AQUA-MODIS sensors, especially in areas with highly variable relief (Cristóbal et al., 2009). The AERONET network is another important source of atmospheric data, but as in the case of radiosonde data, ground network distribution might not be wide enough to provide atmospheric parameters over large areas (Themistocleous et al., 2012). Reanalysis data can also provide atmospheric inputs for atmospheric correction; however, its spatial resolution is still too coarse to be applied to medium resolution imagery.

Several proposals have been made to overcome, at least partially, the difficulties involved in applying radiometric correction in a general way, from the simplest dark-object methods (Chavez, 1988) to other, more complete methods that integrate several factors but keep general feasibility as a basic principle (e.g., Pons and Solé-Sugrañes, 1994, among many others). Nevertheless, times have changed. Together with the availability of near-global detailed DEM, the current free availability of a large part of the Landsat data bank makes it now possible to consider a new paradigm in which medium-high resolution Earth observation data can be used as long time-series for local or global scale studies, such as global forest change (Hansen et al., 2013). Landsat data can be used to gain an understanding of global phenomena using a close-up approach. Indeed, other data with a higher temporal revisit time have a spatial resolution that does not allow to explain some aspects of complex landscapes configured by relief or human history (Pons et al., 2014). This exciting new situation allows new scientific goals to be formulated in a variety of fields, from global change to land planning. However, when we face this possibility, we realize that although there are currently many different radiometric correction methods (Vicente-Serrano et al., 2008), this does not always guarantee radiometric homogeneity in large time-series (Schroeder et al., 2006), which shows that radiometric correction is not completely resolved as yet (Feng et al., 2012), which is especially true for Landsat (Masek et al., 2006). Therefore, current methods have to be revisited in order to be automated in this new era of big data with an important objective to address: to produce series that are "internally" robust while being highly consistent compared to other principal time-series of remote sensing images, such as MODIS (Potapov et al., 2008).

The aim of this work is to revise and improve a previous radiometric (atmospheric, dark-object based, and topographic) correction method (Pons and Solé-Sugrañes, 1994), which has been widely used with Landsat imagery, by using rigorous metadata management that allows automatic radiometric correction of most Landsat imagery while being highly consistent with the Terra-MODIS daily reflectance products. The atmospheric part of the method is improved by accounting for more realistic atmospheric conditions by using pseudoinvariant areas, PIA (Hadjimitsis et al., 2009), generated with 10-year series of Terra-MODIS imagery and polynomial fitting of atmospheric optical depth using MODTRAN simulations, although it would also be possible to use other radiative transfer models currently in use (e.g., 6S, Kotchenova et al., 2006). Other works, such as Gao et al. (2010), have shown that MODIS-like data could be used as a consistent reference for Landsat-like satellite data. The method was then applied automatically in a heterogeneous area, in terms of landscape and relief, over nearly 300 Landsat images from 1984 to 2014 that include different platforms, sensors (MSS, TM and ETM+), processing types and different levels of cloud clover. In other relevant contributions, such as Feng et al. (2013), only imagery practically without clouds was selected (Global Land Survey, GLS); however, using Landsat as a long time-series means that images with cloudy areas need to be included in order to properly carry out, for example, drought monitoring. Finally, surface reflectance will be evaluated through time series robustness, and a spectral signature analysis and image classification over a set of 14 selected images will be carried out. In this paper Landsat-8 imagery was not considered, as in the case of the CDR product (U.S. Geological Survey, 2013), because USGS is still in the process of reviewing its data quality. Future studies for Landsat-8 as well as other platforms (e.g., Sentinel-2) will be carried out in the near future, although we strongly believe that the methodology described here could be easily applied to these new missions.

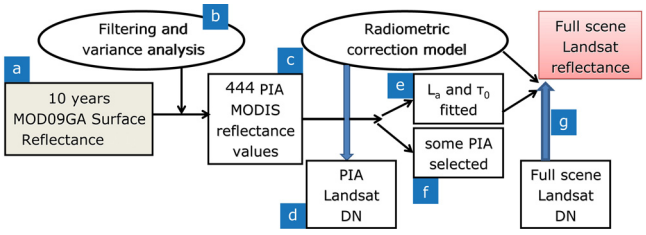

Fig. 1. Flowchart for the proposed methodology, from DN to reflectance values. DN: digital numbers; PIA: pseudoinvariant areas. Letters from *a* to *g* are referenced in the text.

Model presentation

The proposed model (flowchart in Fig. 1) converts from digital number (DN) values to ground reflectances on the solar spectrum at ground level based on the simplified radiometric correction model developed by Pons and Solé-Sugrañes (1994). This method was originally designed for Landsat imagery, although it has also been applied to other platforms and sensors, such as Terra/Aqua-MODIS, SPOT-HRG/HRV, IRS-LISS-III, PROBA-CHRIS or the airborne CASI (Zha et al., 2005; Román-Cuesta et al., 2005; García-Millán et al., 2013). Some applications using this radiometric correction model include forest mapping (Vázquez, 2008; Pérez-Cabello et al., 2010; Zabala and Pons, 2011), crop mapping (Barbosa et al., 1996; Nuarsa et al., 2010; Moré et al., 2011), energy flux modelling (Cristóbal et al., 2011), grassland studies (Zha et al., 2003; Liu et al., 2005), climate-related modelling (Collado et al., 2002), biomass estimation (Lopes et al., 2009; Barrachina et al., 2010), water monitoring (Sánchez et al., 2010; Pons et al., 2012) and forest fire research (Chuvieco et al., 2002; Oliveras et al., 2009), among others.

The model formulation includes topography and atmospheric effects and takes into account several factors, such as relief and solar position (incidence angles and cast shadows), Earth–Sun distance, optical depth, exoatmospheric solar irradiance and sensor calibration parameters. It needs two main inputs: the radiance received by the sensor from an area where there is only (or mainly) atmospheric contribution and the atmospheric optical depth. Other necessary parameters, such as date and time of the image, are read directly from the image metadata or are easily available from external sources.

The model retrieves reflectance at ground level as the simplified radiometric correction model (Pons and Solé-Sugrañes, 1994) in Eq. (1):

$$\rho = \frac{\pi \cdot [L - L_a] \cdot d^2}{\cos\theta \cdot E_0 \cdot \tau_1 \cdot \tau_2} \quad (1)$$

where ρ is the spectral reflectance at ground level, E_0 is the exoatmospheric spectral solar irradiance ($W\,m^{-2}\,\mu m^{-1}$), L is the spectral radiance at sensor level, θ is the incidence angle between the solar vector and the normal vector of the terrain (accounting for its slope and aspect), d is the Sun–Earth distance in astronomical units, L_a is the spectral radiance received by the sensor from an area where there is only atmospheric contribution, τ_1 is the atmospheric transmittance through the path Sun to Earth and τ_2 is the atmospheric transmittance through the path Earth to Sun. τ_1 and τ_2 are both wavelength dependent and calculated according to Eqs. (2) for the Sun to Earth direction and Earth to Sun, (3), respectively:

$$\tau_1 = e^{(\tau_0/\cos(s))} \quad (2)$$

$$\tau_2 = e^{(\tau_0/\cos(v))} \quad (3)$$

where τ_0 is the atmospheric optical depth, s is the illumination zenith angle of the Sun and v is the view zenith angle of the sensor.

As this paper aims to improve and automate the previous radiometric correction model, we would like to explain a modification that has been applied over recent years and that is related to the "Implementation" section of the original paper. It was discussed then how to adapt reflectance values to the 8-bit per pixel and spectral band data type, which was usually used at that time; later on, the solution was to change to using real (float, 4 byte) representations (often in percentage) directly or, for storage saving purposes, using short integer (2 byte) values conveniently scaled after multiplying reflectance values by 10 000. At the same time, this is a general converging solution for the new sensors with higher radiometric resolutions (for example 12 bits in the Landsat-8 Operational Land Imager, OLI, and in the Sentinel-2 Multispectral Imager, MSI). This modification was implemented in the MiraMon GIS & RS software (Pons, 2000) along with other improvements not discussed here (specification of the incidence angle considered not reliable because it exceeds Lambertian limits for most surfaces, detection of cast-shadow pixels, possibility to model the angle of incidence from a DEM of higher resolution than the image, etc.).

The atmospheric part of the model is based on calculating L_a (Eq. (1)) and τ_0 (Eqs. (2) and (3)) for a specific image date and time and for each spectral band. According to Chavez (1988) and Bariou et al. (1986), and in the original model formulation, L_a can be estimated from surfaces that do not receive any direct solar irradiation by using a procedure often referred to as dark object subtraction or the histogram minimum method. We obtained it manually by means of a histogram inspection in order to avoid problems such as false minima in the histogram (for example, due to sensor errors) or approaches based on cumulating a certain percentage of minimum values of the histogram before deciding the L_a to be used. We tried to determine a reasonable minimum in accordance with completely shadowed surfaces (self shadows and cast shadows), or with water bodies in the NIR and, especially, the SWIR. In addition, in the formulation of the original model, τ_0 was considered constant for the full scene (according to, for instance, Dozier, 1989).

However, these procedures can be problematic in some situations. For example, approximating L_a by simple histogram + shadows methods is not convenient in the visible part of the spectrum when there are no hard shadows on the image. Regarding τ_0, it is obvious that a very complex atmospheric situation, e.g. with many clouds, over a large area is extremely difficult to model, but it is also true that in these situations optical remote sensing imagery is not used. Nevertheless, assuming a completely homogeneous atmosphere might be a simplistic approach for many still-useful optical images. For these reasons, the new method improves the estimation of L_a and τ_0 in an automatic procedure, and, like the original, can be applied to most past or future solar spectrum domain imagery, with the exception of those with very high cloud coverage. The main idea is to use the well-known and validated Terra-MODIS time series of reflectance surfaces (Kotchenova and Vermote, 2007; Vermote and Kotchenova, 2008) to detect pseudoinvariant areas (PIA) and to use the reflectance on these areas to estimate L_a and τ_0 for the Landsat scenes to be corrected. In other words, once a data bank of PIA has been obtained for the region of interest, and given a Landsat image in this region, L_a and τ_0 at the time of the satellite pass are estimated for each PIA by fitting Eq. (1) (see section "Pseudoinvariant area (PIA) generation through MODIS imagery" for details). The atmospheric optical depth is initially modelled by means of a third order polynomial function, Eq. (4) for TM and ETM+ sensors and Eq. (5) for MSS sensors, fitted with MODTRAN (2012) mean atmospheric optical depth values computed in transmittance mode with several standard atmospheres (US Standard 1976, MidLattiude Summer, MidLattitude Winter, SubArtic Summer, SubArticWinter and Tropical) and

Table 1
Range of possible values for atmospheric optical depth, L_a thresholds (in W m^{-2} sr^{-1} μm^{-1}) and tolerance reflectances.

		B	G	R	NIR		SWIR1	SWIR2
τ_0 min	TM	0.265	0.212	0.155		0.097	0.053	0.049
	MSS		0.221	0.160	0.141	0.158		
τ_0 max	TM	0.600	0.433	0.337		0.250	0.150	0.105
	MSS		0.453	0.346	0.314	0.350		
L_a min		17.17	7.77	3.64		0.13	−0.84	−0.37
L_a max		37.97	20.75	12.20		5.99	0.09	0.05
Tolerance reflectance		0.017	0.015	0.015		0.023	0.022	0.015

discrete altitude steps of 250 m from 0 to 9000 m; and finally recalculated by adjusting reference values to Eq. (1).

$$\vec{\tau}_h = \begin{pmatrix} \tau_B \\ \tau_G \\ \tau_R \\ \tau_{NIR} \\ \tau_{SWIR1} \\ \tau_{SWIR2} \end{pmatrix} = \begin{pmatrix} 0.524225166047 & -0.000171924013 & 2.4651\times10^{-8} & -1.25\times10^{-12} \\ 0.424690785121 & -0.000142127493 & 2.1028\times10^{-8} & -1.08\times10^{-12} \\ 0.329870334052 & -0.000117419948 & 1.7625\times10^{-8} & -0.91\times10^{-12} \\ 0.240047724024 & -0.000096115185 & 1.4375\times10^{-8} & -0.73\times10^{-12} \\ 0.127035444124 & -0.000048971938 & 0.7141\times10^{-8} & -0.36\times10^{-12} \\ 0.103740066427 & -0.000035915172 & 0.5254\times10^{-8} & -0.27\times10^{-12} \end{pmatrix} \cdot \begin{pmatrix} 1 \\ h \\ h^2 \\ h^3 \end{pmatrix} + \begin{pmatrix} c_B \\ c_G \\ c_R \\ c_{NIR} \\ c_{SWIR1} \\ c_{SWIR2} \end{pmatrix} \quad (4)$$

$$\vec{\tau}_h = \begin{pmatrix} \tau_G \\ \tau_R \\ \tau_{NIR1} \\ \tau_{NIR2} \end{pmatrix} = \begin{pmatrix} 0.444322570590 & -0.000148839670 & 2.1868\times10^{-8} & -1.1210\times10^{-12} \\ 0.338446985809 & -0.000119629348 & 1.7951\times10^{-8} & -0.9266\times10^{-12} \\ 0.308032298646 & -0.000111491404 & 1.6392\times10^{-8} & -0.8353\times10^{-12} \\ 0.347199426572 & -0.000123280911 & 1.6401\times10^{-8} & -0.7680\times10^{-12} \end{pmatrix} \cdot \begin{pmatrix} 1 \\ h \\ h^2 \\ h^3 \end{pmatrix} + \begin{pmatrix} c_G \\ c_R \\ c_{NIR1} \\ c_{NIR2} \end{pmatrix} \quad (5)$$

where τ_h is the atmospheric optical depth for each spectral band, h is the elevation and c is a small additive corrector that is calculated for each band in order to adjust a specific image (date) according to its PIA reflectance values.

Moreover, values of L_a and τ_0 obtained from PIAs are checked with a possible value range. τ_0 thresholds are obtained using the MODTRAN simulations previously explained and L_a thresholds are based on previous experience from several manual corrections under different atmospheric conditions. Therefore, when a value of L_a or τ_0, is over these ranges (Table 1) a specific PIA is not used in a particular correction. This occurs when, on a particular date, the reflectance value is too far (tolerance parameter in Table 1) from the reference value in that PIA (for example because this PIA is under a cloud on the specific date of the image to be corrected).

It is important to note that the proposed model also includes a topographic correction to account for differences in illumination conditions (solar position at the moment of the image acquisition with respect to surface slope, aspect and elevation) and produces similar reflectance responses for similar terrain features (Vanonckelen et al., 2013), which makes it possible to calculate reflectance in high relief areas accurately (Hantson and Chuvieco, 2011). We chose to implement the cosine topographic correction model (Teillet et al., 1982) because it is highly suitable for an automatic methodology like this one. Other methodologies can be more appropriate under optimal conditions but are not suitable for general application. For instance, using a bidirectional reflectance distribution function (BRDF) approach could very convenient because it does not assume a Lambertian response, but as Goslee (2012) states, the necessary information is rarely if ever available, and extremely difficult to obtain for regional or long-term studies. Other advanced methods require knowledge on the different land cover classes or ground reference information, such as for example the phenological stage (Riaño et al., 2003; Hantson and Chuvieco, 2011; Meyer et al., 1993; Vincini and Reeder, 2000), which not available for long time series. The main criticism of cosine correction is that it can produce overcorrection (Zhang and Gao, 2011) in low illumination conditions, when the diffuse irradiance contribution is significant. However, and according to Proy et al. (1989), the Pons and Solé-Sugrañes (1994) methodology discards pixels under incidence angles over 70° as they are considered not to be reliable because they do not usually show Lambertian behaviour for most surfaces. Therefore, by avoiding areas where the Lambertian assumption can hardly be done, overcorrection in these areas is also avoided. Nevertheless, we also tested the effect of the semi-empirical c-correction method (Teillet et al., 1982) in the section devoted to evaluating the method by classification results. In fact, in its original form, c can be derived from the correlation between each band and the cosine of the illumination.

Model application

The model was applied regionally in a heterogeneous area in terms of topography and land cover (see section "Application site"). A total of 291 Landsat scenes from different sensors, processing types and cloud cover were processed, and a DEM was used to run the model (see section "Remote sensing imagery and ancillary data"). PIA were generated through a filtering process of 10-year time-series of the Terra-MODIS daily reflectance product (section "Pseudoinvariant area (PIA) generation through MODIS imagery"). Finally, the model performance was evaluated by calculating the standard deviation along the time series on 30% of the PIA on images corrected automatically and by comparing image classification and spectral signatures over a 14 image evaluation set (see section "Model evaluation: time series robustness, spectral signatures and image classification").

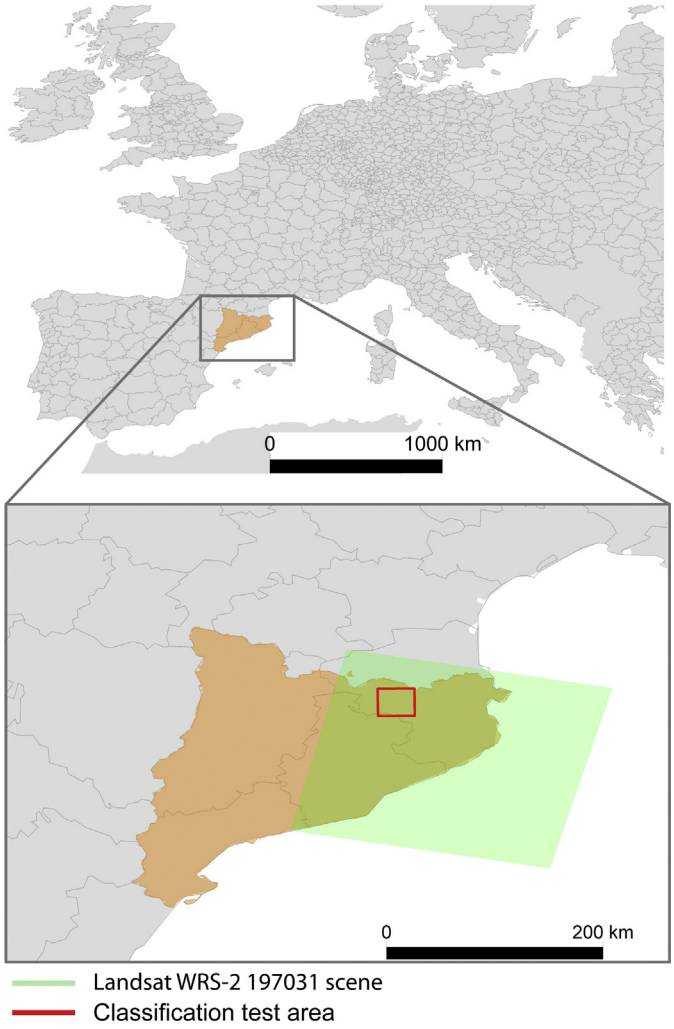

Fig. 2. Study area and model evaluation area. The green rectangle is the Landsat WRS2 197-031 scene. The red rectangle is the area where the classification evaluation was applied. (For interpretation of the references to colour in this figure legend, the reader is referred to the web version of the article.)

Application site

The 20 000 km^2 study area is located in Catalonia, in the north-east of the Iberian Peninsula (Fig. 2), matching the 197-031 path and row in the Worldwide Reference System-2 (WRS-2) used to distribute Landsat 4–7 full frames. The centre of the scene is approximately 2°40′E 41°40′N. The illumination conditions throughout the year are quite different due to latitude (solar elevation angles range from 20.5° to 61.4° at the time of the satellite pass). The area alternates between mountains and plains with a mean elevation of around 700 m a.s.l, ranging from 0 to 3000 m a.s.l. The rugged surface terrain makes the zone interesting for considering topographic effects on radiometric correction methods. The study area is also composed of different land cover types in a heterogeneous landscape, such as crops, perennial and deciduous woods, shrub areas, urban areas and inland waters, which also makes the site interesting for classification and spectral signature purposes.

Remote sensing imagery and ancillary data

The radiometric correction model was run over 291 Landsat images from the 197-031 path and row (see green area in Fig. 2) obtained between 1984 and 2014 (see Table 2). In order to evaluate the performance of the model, 14 Landsat images were selected considering a wide range of situations based on cloud cover (up to 60%), processing type, format distribution, sensor, spectral signature and classification and image metadata (see Table 3). Image metadata, such as scale and offset parameters to convert from DN to radiance, as well as date/time to compute illumination conditions, are especially important for automating the radiometric process. Therefore, correct metadata treatment is necessary due to the differences in metadata formats between different image distributors and different software capabilities (Pons, 2000; Zabala and Pons, 2002; Pesquer et al., 2012). Landsat images distributed by the United States Geological Survey (USGS) were downloaded from the EarthExplorer website (http://earthexplorer.usgs.gov), and European Space Agency (ESA) images were available from a previous project (Pons et al., 2012) and completed with an ESA image request (research project 10837). Landsat CDR products, used in the results validation section, were also downloaded from the EarthExplorer website.

In order to generate the PIA, a 10-year time-series, from 2002 to 2011, of the Terra-MODIS daily surface reflectance product (MOD09GA) was downloaded from the NASA Earth Observing System Data and Information System (http://reverb.echo.nasa.gov/reverb/) (step *a* in flowchart Fig. 1). Terra-MODIS reflectance bands similar to Landsat (see Table 4) at 500 m spatial resolution were processed.

Finally, to run the topographic correction of the model, we used a DEM of 15 m spatial resolution (MET-15) from the Institut Cartogràfic de Catalunya (ICC, 2011).

Pseudoinvariant area (PIA) generation through MODIS imagery

PIA were generated through the Terra-MODIS surface reflectance product (MOD09GA) at 500 m spatial resolution. This is a very feasible product (Justice et al., 2002), widely used and referenced in the literature for research and applications (e.g., Maier, 2010; Yi et al., 2008). In addition, it has some advantages that make it suitable for generating PIA for Landsat radiometric correction, such as having a similar spectral configuration (see Table 4) and a similar image acquisition time as Landsat platforms,

Table 2
Summary of the nearly 300 Landsat images processed from the path-row 197-031; these images were obtained between 1984 and 2014.

Platform	Sensor	Distributor	Type of processing	Number of images	Total
Landsat 5	MSS	USGS	NLAPS	2	14
			LPGS	12	
Landsat 4	TM	USGS	LPGS	7	8
Landsat 4	TM	USGS	NLAPS	1	
Landsat 5	TM	USGS	LPGS	75	146
Landsat 5	TM	ESA	CEOS	71	
Landsat 7	SLC-on	USGS	LPGS	33	123
Landsat 7	SLC-on	ESA	CEOS	9	
Landsat 7	SLC-off	USGS	LPGS	81	

Table 3
List of images used to perform different evaluations of the radiometric correction (see "Main role" column). These images were selected from the nearly 300 images of Table 2.

Date (yyyy-mm-dd)	Distributor	Type of processing	Platform	Sensor	Main role
1984-06-03	USGS	LPGS	Landsat 5	MSS	Type of processing
1985-07-24	USGS	NLAPS	Landsat 5	TM	Type of processing
1991-07-01	USGS	NLAPS	Landsat 4	TM	Type of processing
2001-09-30	USGS	LPGS	Landsat 7	ETM+	Cloud cover
2003-02-08	ESA	CEOS	Landsat 7	ETM+	Type of processing
2004-09-30	ESA	CEOS	Landsat 5	TM	Spectral signature and classification
2005-04-26	ESA	CEOS	Landsat 5	TM	Spectral signature and classification
2005-05-28	ESA	CEOS	Landsat 5	TM	Spectral signature and classification
2005-06-29	ESA	CEOS	Landsat 5	TM	Spectral signature and classification
2008-06-13	USGS	LPGS	Landsat 7	ETM+	Cloud clover + SLC-off
2011-03-10	USGS	LPGS	Landsat 5	TM	Classification
2011-04-11	USGS	LPGS	Landsat 5	TM	Classification
2011-05-29	USGS	LPGS	Landsat 5	TM	Classification
2011-10-04	USGS	LPGS	Landsat 5	TM	Classification

Table 4
Correspondence of spectral bands between Terra-MODIS (Feng et al., 2013) and Landsat TM, ETM+ and MSS (Chander et al., 2009).

Band	Landsat (MSS) TM/ETM+ band number	MSS spectral range (nm) (Landsat 4–5)	TM spectral range (nm)	ETM+ spectral range (nm)	MODIS band number	MODIS spectral range (nm)
B	1		450–520	450–515	3	459–479
G	(1)2	497–607	520–600	525–605	4	545–565
R	(2)3	603–696	630–690	630–690	1	620–670
NIR	(3)4	701–813	760–900	750–900	2	841–876
	(4)	808–1023				
SWIR1	5		1550–1750	1550–1750	6	1628–1652
SWIR2	7		2080–2350	2090–2350	7	2105–2155

which minimizes differences in atmospheric and illumination conditions (Feng et al., 2012).

In order to ensure the highest PIA quality, a selection of available MODIS surface reflectance images was made by applying the methodology developed in Pesquer et al. (2013a) based on two criteria: quality masks and reasonable acquisition geometry, and a geostatistical spatial pattern analysis using variograms. In addition, a new, third criterion based on illumination conditions was included in the present work. Indeed, in the original methodology, image pixels were selected according to quality masks (when snow, fire or cloud flags were not present the product was considered of ideal quality) and images with a sensor zenith angle higher than 35° were excluded. The second criterion was used to detect statistical image anomalies through a spatial pattern model obtained from variogram analysis; previous works demonstrated the potential uses of geostatistical tools for analysing spatial patterns (Garrigues et al., 2007; Wallace et al., 2000) as well as for image quality assessment (Pesquer et al., 2013b). In the third, new criterion, illumination conditions were taken into account through a DEM (Wilson and Gallant, 2000; Veraverbeke et al., 2010) in order to avoid both cast shadow pixels and pixels under an incidence angle higher than 70° (Proy et al., 1989), considered to be not reliable because they do not usually show Lambertian behaviour for most surfaces. Nevertheless, the condition of being pseudoinvariant means that the selected PIA are mostly located in non-rugged areas; therefore, combining the two illumination correction protocols makes PIA even more comparable to Landsat imagery. After these three criteria were applied to MODIS imagery (step *b* in flowchart Fig. 1), a mean image and a standard deviation image were computed for the 10-year period.

A PIA should show almost constant reflectance values for long time periods. In this study we selected PIA by choosing those pixels that have low standard deviation reflectance values in the image of the standard deviation of the 10-year MODIS series. According to Feng et al. (2013) these thresholds should not be the same for all MODIS bands, and a new set of thresholds has been defined for each band (Table 5).

Model evaluation: time series robustness, spectral signatures and image classification

291 Landsat images from the MSS, TM and ETM+ sensors were used to evaluate the performance of the automatic radiometric correction. These images were obtained between 1984 and 2014 and distributed by different agencies (ESA and USGS) and in different formats (see Table 2). This time series was produced by using, to fit the model, a 70% of the total PIA available, while the remaining 30% of PIA were used to evaluate the time series robustness; in these last PIA, variations in reflectance were computed along the series.

Moreover, using the 14 Landsat image evaluation set (see Table 3), reprocessed using all of the PIA to fit the model, we produced a land cover map of the natural areas, created by classification, and spectral signatures were extracted from the radiometrically corrected Landsat imagery. In the classification, based on the methodology proposed by Serra et al. (2003) and previously applied to other areas (Moré et al., 2007; Serra et al., 2009; Zabala and Pons, 2011; Pons et al., 2012), results were compared to the classification obtained using imagery corrected by the previous method (non-automatic, and where the atmospheric optical depth is a constant) and to the classification obtained using the USGS product (when it exists). Two classifications using two sets of images (2011-03-10, 2011-04-11, 2011-05-29, 2011-10-04 and 2004-09-30, 2005-04-26, 2005-05-28, 2005-06-29) were produced. Input variables were Landsat solar bands and NDVI and greenness and wetness Tasseled Cap components (Kauth and Thomas, 1976) for each date, using a total of 36 images for each classification. The accuracy was tested through independent test areas (Campbell, 1996). Classifications were mainly focused on natural vegetation categories (legend in Fig. 7) in a subregion of the study area measuring 25 km × 25 km, located in a mountain region, heterogeneous in terms of covers and relief (see red rectangle in Fig. 2).

In addition to image classification, spectral signatures were extracted from Landsat imagery (see Table 3) and compared to the MODIS reflectance product to evaluate signature coherence. A

Table 5
Maximum standard deviation (in reflectance units x10^4, typical for MODIS reflectance products) to be considered as a pseudoinvariant pixel.

	B	G	R	NIR	SWIR1	SWIR2
Standard deviation	241	199	193	270	309	212

Table 6
Number of PIA used per date and Landsat band. B: blue, G: green, R: red, NIR: near infrared, SWIR*: short wave infrared for TM and ETM+, and NIR2 for MSS.

Date	B	G	R	NIR	SWIR1*	SWIR2
1984-06-03		45	75	21	120	
1985-07-24	17	23	55	147	296	218
1991-07-01	7	133	113	100	190	164
2001-09-30#	11	135	144	216	222	216
2003-08-02	3	201	249	173	285	279
2004-09-30	15	212	264	277	240	223
2005-04-26	274	279	281	285	286	273
2005-05-28	239	300	304	308	309	308
2005-06-29	175	265	264	280	284	278
2008-06-13#	8	31	54	73	102	92
2011-03-10	34	263	203	266	284	280
2011-04-11#	204	281	280	287	289	289
2011-05-29	79	226	219	158	264	258
2011-10-04	1	65	251	257	291	290

Fig. 3. Monthly distribution of Terra-MODIS best quality images from 2002 to 2011.

total of 14 sites with a mean area of 63 ha and at least the area of the MODIS pixel size (500 m × 500 m) corresponding to four representative land cover types (Aleppo pine, Holm oak tree, Scots pine and urban) were selected using the Land Cover Map of Catalonia (MCSC3, 2005). It was ensured that these areas did not belong to any PIA used to run the radiometric correction.

We also considered to check results through the Landsat–MODIS Consistency Checking System (LMCCS, Feng et al., 2012), but we could not adopt it easily because we used images in different formats and from different processing chains.

Results and discussion

Metadata and image processing type

A total of 291 images from several Landsat platforms (Landsat-4, Landsat-5 and Landsat-7) and sensors (MSS, TM and ETM+) using USGS and ESA file formats and processing chains were automatically corrected (see Table 1 and step *g* in flowchart Fig. 1). As previously stated, metadata are essential to properly correct remote sensing imagery, especially to avoid errors if an automatic radiometric correction is applied. From the beginning of the Landsat programme, different file formats have been used to distribute Landsat imagery, such as CEOS, GeoTIFF and NDF. These distribution formats depend on the source of acquisition, pre-processing level and processing date; this is also true for the metadata files, which often change (Pons et al., 2012; Feng et al., 2012). In addition, these formats are associated with different Landsat image processing systems, particularly with NLAPS and LPGS in the USGS case (Cristóbal et al., 2009). Although the Landsat image distributors continually refine image and metadata distribution, in some of the processed imagery there is a lack of coherence between image metadata and values in the literature, especially regarding DN to radiances conversion. Therefore, an important part of this work was to read multiple formats and to ensure proper metadata handling in order to apply the most appropriate values according to those in the literature to avoid further errors caused by these kinds of discrepancies.

Pseudoinvariant areas (PIA) and atmospheric optical depth

A total of 124 MODIS images (specified in Appendix 1) fulfilling the PIA filtering criteria from 2002 to 2011 and reproducing a

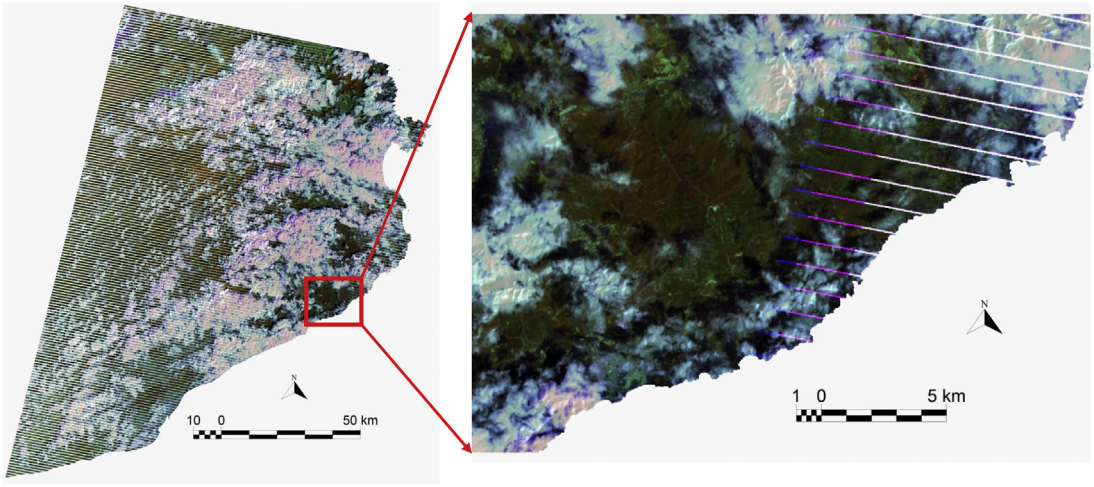

Fig. 4. Landsat-7 ETM+ 4,5,3 RGB composite from 2008-06-13 image after a radiometric correction under very high cloud cover and SLC-off artefacts.

Table 7
Statistics of the time series robustness analysis in % reflectance units. Note that these values are, in all cases, lower than the deviations indicated by Feng et al. (2013).

	B	G	R	NIR	SWIR	SWIR2
Average absolute deviation about median	0.54%	0.68%	0.69%	1.81%	1.56%	0.96%

seasonal phenology were selected (see Fig. 3). A total of 444 PIA of 500 m × 500 m were obtained by applying the thresholds from Table 5 to these 124 images (step *c* in flowchart Fig. 1). Then, and according to the proposed methodology, Eq. (1) was applied to each PIA for each Landsat band and date (step *d* in flowchart Fig. 1) in order to fit L_a and τ_0 parameters. In all cases, Table 1 thresholds were guaranteed discarding those Landsat images that, when fitting L_a and τ_0 (step *e* in flowchart Fig. 1), implied exceeding reasonable thresholds.

The number of PIA used in each radiometric correction is different depending on the band and date (see Table 6 and step *f* in flowchart Fig. 1) due to different image atmospheric conditions. From the image evaluation set, 12 images were successfully corrected with a default tolerance reflectance. However, in two ETM+ images (2001-09-30 and 2008-06-13 flagged with # in Table 6 and Fig. 4) and one TM image (2011-04-11), it was necessary to increase (1.5 factor) the tolerance threshold (Table 1). Indeed, the combination of high cloud cover (27% and 58%, respectively) and SLC-off artefacts meant that the minimum number of PIA for a numerical solution was not obtained. Therefore, in scenes where PIA are hard to find, a reference-based approach (Gao et al., 2010) can be applied. However, in the case of having images with a high cloud percentage, tolerance could be augmented to correct the cloudless

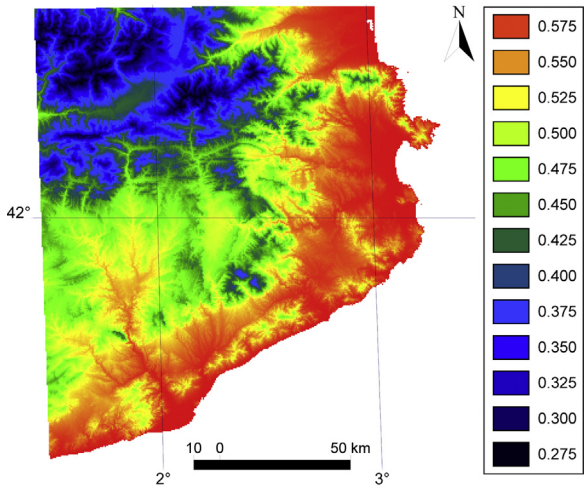

Fig. 5. Atmospheric optical depth computed as a function of elevation for the 2011-05-29 image.

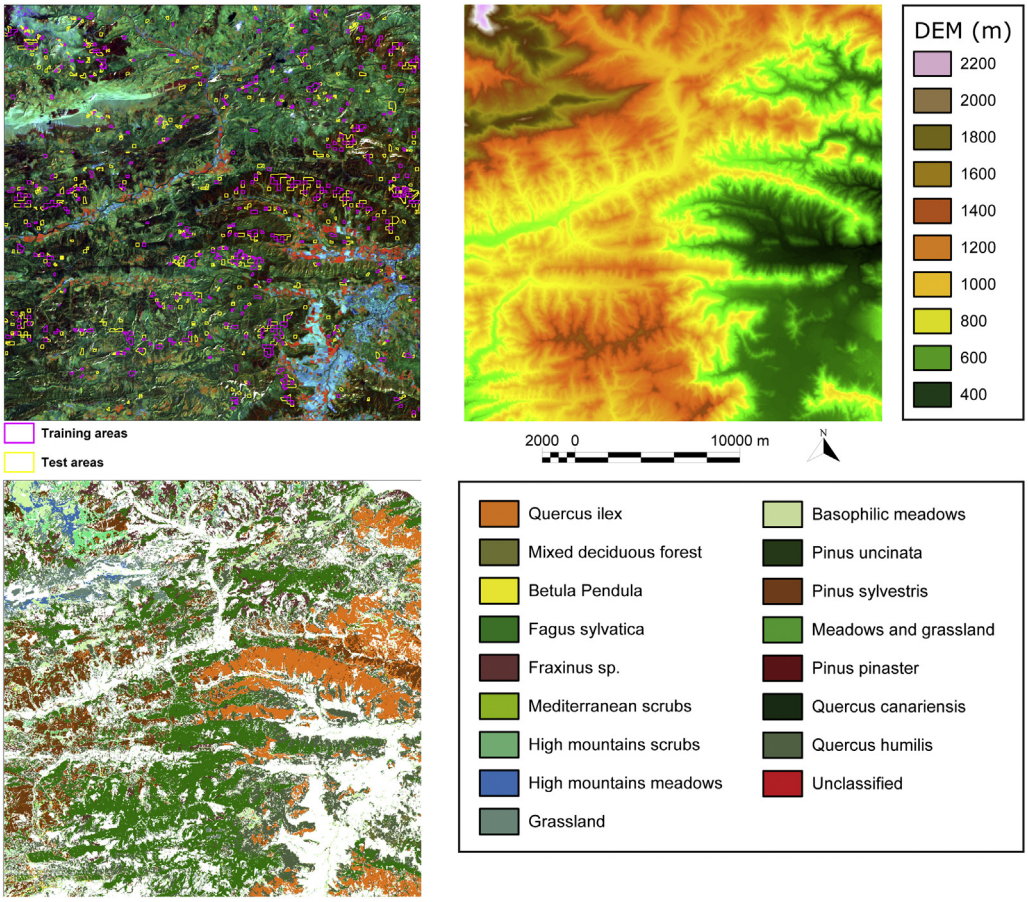

Fig. 6. Upper-Left panel: 4-5-3 RGB composite of the reflectance product generated by the automatic method on 26-April-2005, including fitting and test areas used for classification. Upper-Right panel: DTM of the study area. Lower-Left panel: result of the classification of natural areas using the new reflectance product.

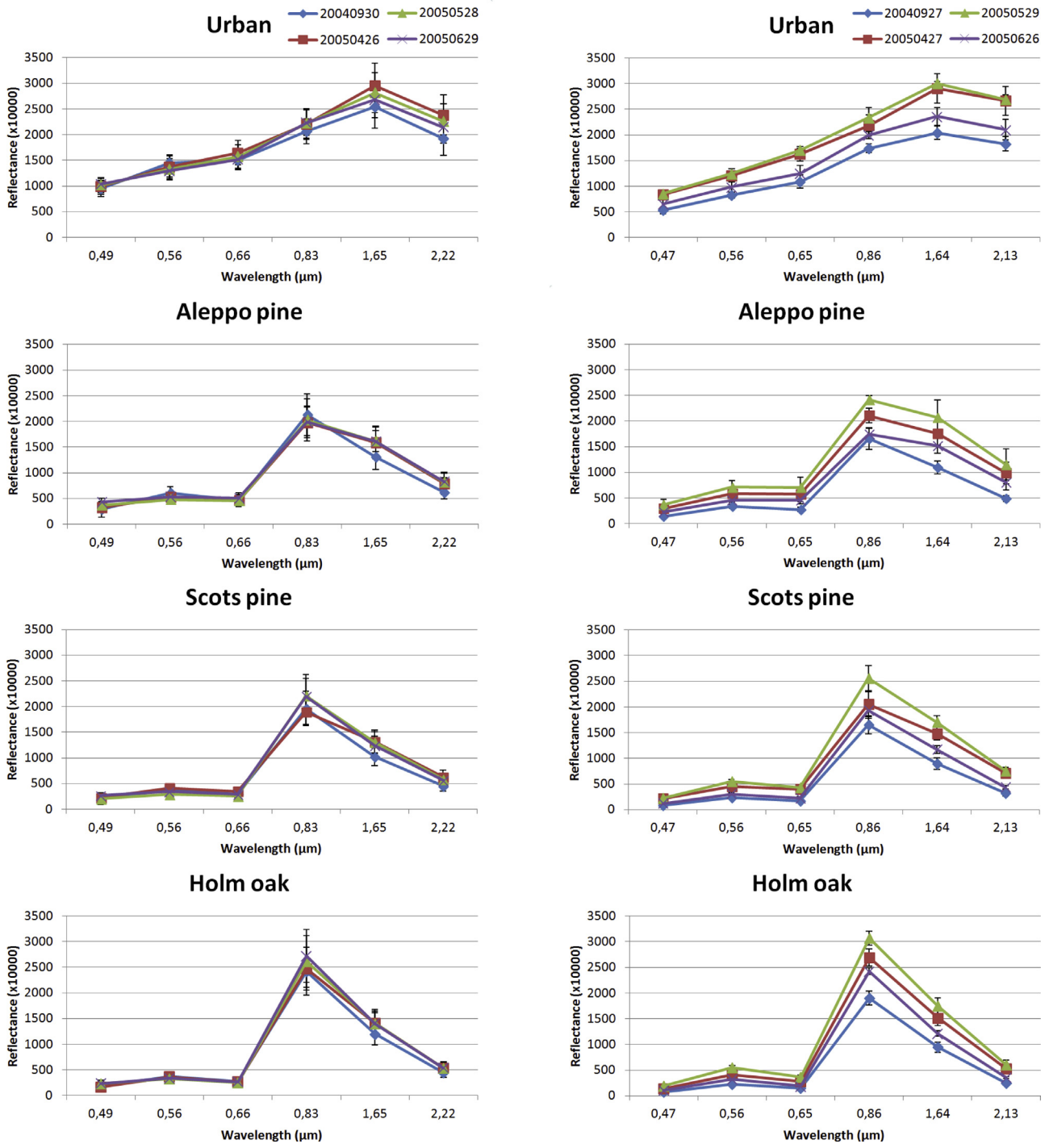

Fig. 7. Spectral signatures of four different categories and four different dates comparing the Landsat automatic radiometric correction (left column) and the MODIS reflectance product (right column). Note that these signatures have not been determined over MODIS pseudo-invariant areas.

parts of the image. This is especially useful when long time-series of remote sensing imagery are needed, such as in drought analysis (Domingo et al., 2013). Because the proposed method is automatic, image metadata were updated to keep the user informed about the applied tolerance and, consequently, about the potential radiometric correction quality.

Finally, determining c, the small additive corrector in Eq. (4) based on PIA reference values, allows the continuous model of the atmospheric optical depth to be adapted to each Landsat band and date, resulting in a more detailed estimation of the atmospheric optical depth (see Fig. 5).

Time series robustness

In order to evaluate the robustness of the method, reflectance values along the time series were randomly split into two groups: 70% of them were used to fit the model, while the remaining 30% were used for testing purposes. A total dataset of 291 Landsat

Table 8
Comparison of the global accuracy of the 2011 classifications generated by the manual and automatic methods and by the CDR product.

2011	Automatic	Manual	CDR
Global accuracy	77.80%	76.20%	73.90%

images from different sensors between 1984 and 2014 were then processed (see Table 2). From this dataset, 214 images were successfully corrected, 174 using the default reflectance tolerance and 40 by slightly increasing (1.5) this range. The remaining 77 images (26%) could not be corrected mainly because of the heavy cloud coverage.

30% of PIA were used for testing purposes because they provide the reflectance on these areas over the corrected Landsat images and these reflectance time series should have a minimum variation. For each PIA pixel, its average absolute deviation about median was calculated along the whole time series for each spectral band; only PIA with 20 or more dates over the time series were used.

The results (Table 7) show that these deviations are 1.04% on average along the series, having its minimum in the blue band and its maximum in the NIR band, and are always under the thresholds of PIA deviation defined in Table 5 according to Feng et al. (2013). This therefore demonstrates the robustness of the correction method over time. These results suggest that perhaps the thresholds could be narrower so that reflectances that are even more stable would be obtained in PIA.

Classification

Two classifications were generated from three different radiometric correction methods: Pons and Solé-Sugrañes (1994) (called "manual" in Tables 8 and 9), the USGS product (called "CDR" in Table 8) and the proposed automatic method (called "automatic" in Tables 8 and 9). The results in Table 8 and Fig. 6, obtained from an independent set of test areas, show that the accuracy of the maps obtained from the imagery corrected by any of these three methods is similar. Moreover, in the two classification sets (2004/2005 and 2011), the automatic methodology improves the manual classification probably due the new, vertically heterogeneous model of the atmospheric optical depth and the more objective determination of L_a. This means that the new method is at least as robust as the original manual method, and makes it possible to correct large volumes of Landsat imagery automatically without any manual supervision once PIA are generated.

In addition, a comparison between two topographic methods, cosine and the *c*-correction, were applied for this previous 2011 example of classification. In this case, the global accuracy obtained by applying the *c*-correction is 76.30% for the 2011 period, less than when the cosine method was applied, and 82.70%, for the 2004-05, which is very similar to the cosine approach. This good performance of cosine with respect to the *c*-correction is mainly caused by two factors: by avoiding non-Lambertian responses in large incidence angles, pixels usually benefitted by the *c*-correction were excluded and, moreover, fitting of the *c* parameter could be negatively affected by clouds and snow cover in the correlation step that generates the slope and offset parameters needed to compute it (the case in the 2011 image).

Table 9
Comparison of the global accuracy of the 2004/2005 classifications generated by the manual and automatic methods.

2004–2005	Automatic	Manual
Global accuracy	82.50%	80.10%

Spectral signatures

MODIS and Landsat spectral signatures were compared to evaluate the radiometric correction. Spectral signatures of four categories that were representative of the study area (Urban, Aleppo pine (*Pinus halepensis*), Scots pine (*Pinus sylvestris*) and Holm oak (*Quercus ilex*)) were extracted from several polygons with a minimum area of 28 ha, and a mean reflectance value was computed. Results are similar to those obtained from MODIS, but are more coherent in the Landsat corrected series when different dates are compared (see Fig. 7) (all forests are evergreen). However, when deviations inside each date are compared, MODIS shows lower values probably because of its larger pixel size, which produces more "averaged" figures between the different pixels of the signature polygon for a specific date.

Conclusions

An improved and automated radiometric correction method based on Pons and Solé-Sugrañes (1994) has been successfully evaluated and ground surface reflectances were obtained for different types of Landsat platforms (Landsat-4, 5 and 7), sensors (MSS, TM and ETM+), formats and processing types (LPGS, NLAPS, CEOS) and even in images with high cloud cover and SCL-off artefacts (Landsat-7). The proposed methodology has demonstrated to be fully automatic, from the selection of the best quality MODIS reference images and the generation of pseudoinvariant areas (PIA) to the retrieval of coherent ground surface reflectances. About 300 Landsat images were processed without using any auxiliary meteorological or atmospheric products and not requiring dark objects or dense vegetation areas. The methodology proved to be useful to obtain long time-series of robust imagery. It is worth noting that the PIA concept can also be applied to other platforms with similar band configurations, such as SPOT high resolution instruments (HRG, HRVIR or HRV) and the VEGETATION instrument, adapting model equations when required. Evaluation results showed good visual agreement between the MODIS and Landsat spectral signatures, and classification results yielded better quality images corrected with the new automatic radiometric correction method than those obtained with the original manual method or the CDR products. The new method also demonstrated that it is feasible to automatically correct large volumes of Landsat imagery from automatically generated PIA without any manual supervision. Moreover, images can be corrected for a wide variety of situations, providing a larger databank for our area than the CDR product currently does.

We would like to emphasize that this simplified approach is not intended to substitute highly precise radiometric corrections made when more detailed topographic or atmospheric information is available, but rather offers a reasonably good procedure for the new era of long time-series of global remote sensing data. Future work will be focused on the implementation of this automatic radiometric correction method for Landsat-8, SPOT and Sentinel-2 data.

Acknowledgments

This work was partially supported by the Catalan Government under Grant SGR2009-1511, by the Spanish Ministry of Economy and Competitiveness and the European regional development fund (ERDF) under Grant CGL2012-33927 (DinaCliVe). We are very grateful to the USGS policy about Landsat data; the project has also used data provided by the European Space Agency under the ESA research project 10837. Xavier Pons is a recipient of an ICREA Academia Excellence in Research Grant (2011–2015).

Appendix A.

List of the 124 images (MODIS Terra MOD09GA product) selected for generating pseudoinvariant areas. They are grouped by year.

- 20020615; 20020622; 20020814; 20020915; 20020926
- 20030208; 20030312; 20030321; 20030406; 20030614; 20030625; 20030630; 20030711; 20030718; 20030803; 20030810; 20030918; 20031105
- 20040213; 20040424; 20040618; 20040722; 20040814; 20040922; 20040927;
- 20050213; 20050319; 20050427; 20050506; 20050525; 20050529; 20050626; 20050716; 20050806; 20050831; 20051223;
- 20060104; 20060126; 20060207; 20060214; 20060228; 20060302; 20060311; 20060327; 20060331; 20060412; 20060509; 20060519; 20060525; 20060601; 20060608; 20060613; 20060619; 20060624; 20060703; 20060710; 20060721; 20060726; 20060731; 20060804; 20060809; 20060903; 20060910; 20061007; 20061028; 20061030; 20061106; 20061110; 20061212; 20061226; 20061228; 20061231;
- 20070314; 20070424; 20070508; 20070602; 20070706; 20070715; 20070805; 20070828; 20070901; 20070906; 20071019; 20071102;
- 20080208; 20080222; 20080302; 20080314; 20080622; 20080701; 20080720; 20080724; 20080731; 20080805; 20080915; 20081005;
- 20090226; 20090314; 20090319; 20090718; 20090723; 20090817; 20090821; 20090906; 20090929; 20091013;
- 20100520; 20100621; 20100705; 20100714; 20100930; 20101007; 20101018;
- 20110205; 20110307; 20110401; 20110412; 20110622; 20110627; 20110811; 20110823; 20110910; 20111003; 20111010; 20111026.

References

Barbosa, P.M., Casterad, M.A., Herrero, J., 1996. Performance of several Landsat 5 Thematic Mapper (TM) image classification methods for crop extent estimates in an irrigation district. Int. J. Remote Sens. 17, 3665–3674.

Bariou, R., Lecamus, D., Le Henaff, F., 1986. Corrections Radiometriques. Presses Universitaires de Rennes 2, Rennes.

Barrachina, M., Cristóbal, J., Tulla, A.F., 2010. Los recursos ganaderos en los sistemas extensivos de la montaña pirenaica catalana: aproximación al cálculo de la biomasa herbácea mediante el uso de la Teledetección. Serie Geográfica 16, 35–49.

Campbell, J.B., 1996. Introduction to Remote Sensing, second ed. Taylor and Francis, London.

Chander, G., Markham, B.L., Helder, D.L., 2009. Summary of current radiometric calibration coefficients for Landsat MSS, TM, ETM+, and EO-1 ALI sensors. Remote Sens. Environ. 113, 893–903.

Chavez, P.S., 1988. An improved dark-object subtraction technique for atmospheric scattering correction of multispectral data. Remote Sens. Environ. 24, 459–479.

Chuvieco, E., Riaño, D., Aguado, I., Cocero, D., 2002. Estimation of fuel moisture content from multitemporal analysis of Landsat Thematic Mapper reflectance data: applications in fire danger assessment. Int. J. Remote Sens. 23, 2145–2162.

Collado, A.D., Chuvieco, E., Camarasa, A., 2002. Satellite remote sensing analysis to monitor desertification processes in the crop-rangeland boundary of Argentina. J. Arid Environ. 52, 121–133.

Cristóbal, J., Jiménez-Muñoz, J.C., Sobrino, J.A., Ninyerola, M., Pons, X., 2009. Improvements in land surface temperature retrieval from the LANDSAT series thermal band using water vapour and air temperature. J. Geophys. Res.: Atmos., 11.

Cristóbal, J., Poyatos, R., Ninyerola, M., Llorens, P., Pons, X., 2011. Combining remote sensing and GIS climate modelling to estimate daily forest evapotranspiration in a Mediterranean mountain area. Hydrol. Earth Syst. Sci. 15, 1563–1575.

Domingo, C., Cristóbal, J., Ninyerola, M., Pons, X., 2013. MODIS time series analysis as a tool for forest drought detection in Catalonia (NE Iberian Peninsula): integration of remote sensing and climatic variables. Geophysical Research Abstracts 15, EGU2013-10300. EGU General Assembly 2013.

Dozier, J., 1989. Spectral signature of Alpine snow cover from the Landsat Thematic Mapper. Remote Sens. Environ. 28, 9–22.

European Spatial Agency, 2005. Landsat ETM/TM CEOS/ESA Products, The internet: http://earth.esa.int/pub/ESA_DOC/Landsat_FAQ.pdf (accessed 02.01.14).

Feng, M., Huang, C., Channan, S., Vermote, E.F., Masek, J.G., Townshend, J.R., 2012. Quality assessment of Landsat surface reflectance products using MODIS data. Comput. Geosci. 38, 9–22.

Feng, M., Sexton, J.O., Huang, C., Masek, J.G., Vermote, E.F., Gao, F., Narasimhan, R., Channan, S., Wolfe, R.E., Townshend, J.R., 2013. Global surface reflectance products-from Landsat-Assessment using coincident MODIS observations. Remote Sens. Environ. 134, 276–293.

Franklin, S.E., Giles, P.T., 1995. Radiometric processing of aerial and satellite remote-sensing imagery. Comput. Geosci. 21, 413–423.

Gao, F., Masek, J., Wolfe, R., Huang, C., 2010. Building consistent medium resolution satellite data set using moderate resolution imaging spectroradiometer products as reference. J. Appl. Remote Sens. 4, 043526, http://dx.doi.org/10.1117/1.3430002.

García-Millán, V., Sánchez-Azofeifa, G.A., Malvárez, G.-C., Moré, G., Pons, X., Yamanaka-Ocampo, M., 2013. Effects of topography on the radiometry of CHRIS/PROBA images of successional stages within tropical dry forests. IEEE J. Select. Top. Appl. Earth Observ. Remote Sens. 6, 1584–1595.

Garrigues, S., Allard, D., Baret, F., 2007. Using first and second order variograms for characterizing landscape spatial structures from remote sensing imagery. IEEE Trans. Geosci. Remote Sens. 45, 1823–1834.

Goward, S.N., Masek, J.G., 2001. Editorial: Landsat-30 years and counting. Remote Sens. Environ. 78, 1–2.

Goslee, S.C., 2012. Topographic corrections of satellite data for regional monitoring. Photogram. Eng. Remote Sens. 78 (9), 973–981.

Hadjimitsis, D.G., Clayton, C.R.I., Retalis, A., 2009. The use of selected pseudo-invariant targets for the application of atmospheric correction in multi-temporal studies using satellite remotely sensed imagery. Int. J. Appl. Earth Observ. Geoinform. 11, 192–200.

Hale, S.R., Rock, B.N., 2003. Impact of topographic normalization on land-cover classification accuracy. Photogram. Eng. Remote Sens. 69, 785–791.

Hansen, M.C., Potapov, P.V., Moore, R., Hancher, M., Turubanova, S.A., Tyukavina, A., Thau, D., Stehman, S.V., Goetz, S.J., Loveland, T.R., Kommareddy, A., Egorov, A., Chini, L., Justice, C.O., Townshend, J.R.G., 2013. High-resolution global maps of 21st-century forest cover change. Science 342 (6160), 850–853.

Hantson, S., Chuvieco, E., 2011. Evaluation of different topographic correction methods for Landsat imagery. Int. J. Appl. Earth Observ. Geoinform. 13, 691–700.

ICC, 2011. Especificacions tècniques Revisió de document 2 - Juny 2011 del Model d'Elevacions del Terreny de Catalunya 15x15 metres (MET-15). Institut Cartogràfic de Catalunya, The internet: http://www.icc.cat/cat/content/download/12339/41446/file/met15v20esp_02ca.pdf (accessed 02.01.14).

Janzen, D.T., Fredeen, A.L., Wheate, R.D., 2006. Radiometric correction techniques and accuracy assessment for Landsat TM data in remote forested regions. Can. J. Remote Sens. 32, 330–340.

Justice, C.O., Townshend, J.R., Vermote, E.F., Masuoka, E., Wolfe, R.E., Saleous, N., Roy, D.P., Morisette, J.T., 2002. An overview of MODIS Land data processing and product status. Remote Sens. Environ. 83, 3–15.

Kauth, R.J., Thomas, G.S.,1976. The tasseled Cap. A Graphic Description of the Spectral-Temporal Development of Agricultural Crops as Seen by LANDSAT. In: Proceedings of the Symposium on Machine Processing of Remotely Sensed Data. Purdue University of West Lafayette, Indiana, 4B41–4B51.

Kotchenova, S.Y., Vermote, E.F., Matarrese, R., Klemm Jr., F.J., 2006. Validation of a vector version of the 6S radiative transfer code for atmospheric correction of satellite data. Part I: Path radiance. Appl. Opt. 45 (26), 6762–6774.

Kotchenova, S.Y., Vermote, E.F., 2007. Validation of a vector version of the 6S radiative transfer code for atmospheric correction of satellite data. Part II. Homogeneous Lambertian and anisotropic surfaces. Appl. Opt. 46 (20), 4455–4464.

Liu, Y.S., Hu, Y.C., Peng, L.Y., 2005. Accurate quantification of grassland cover density in an alpine meadow soil based on remote sensing and GPS. Pedosphere 15, 778–783.

Lopes, D.M., Aranha, J.T., Walford, N., O'Brien, J., Lucas, N., 2009. Accuracy of remote sensing data versus other sources of information for estimating net primary production in Eucalyptus globulus Labill. and Pinus pinaster Ait. ecosystems in Portugal. Can. J. Remote Sens. 35, 37–53.

Maier, S.W., 2010. Changes in surface reflectance from wildfires on the Australian continent measured by MODIS. Int. J. Remote Sens. 31, 3161–3176.

Masek, J., Vermote, E., Saleous, N., Wolfe, R., Hall, F., Huemmrich, K.F., Gao, F., Kutler, J., Lim, T., 2006. A Landsat surface reflectance dataset for North America, 1990–2000. IEEE Geosci. Remote Sens. Lett. 3, 68–72.

Meyer, P., Itten, K.I., Kellenbenberger, T., Sandmeier, S., Sandmeier, R., 1993. Radiometric corrections of topographically induced effects on Landsat TM data in an alpine environment. ISPRS J. Photogram. Rem. Sens. 48, 17–28.

MCSC3, 2005. Land Cover Map of Catalonia, 3rd edition, version 2 (2005–2007), The Internet: http://www.creaf.uab.es/mcsc/usa/index.htm (accessed 02.01.14).

MODTRAN, 2012. MODerate resolution atmospheric TRANsmission: Narrow band model atmospheric radiative transfer code, v. 5, The Internet: http://www.modtran5.com (accessed 02.01.14).

Moré, G., Serra, P., Pons, X., 2007. Improvements on classification by tolerating nodata values – application to a hybrid classifier to discriminate Mediterranean vegetation with a detailed legend using multitemporal series of images. In: IEEE International Geoscience and Remote Sensing Symposium, IGARSS, vol. 1, Denver, CO, United States 4241201, pp. 192–195.

Moré, G., Serra, P., Pons, X., 2011. Multitemporal flooding dynamics of rice fields by means of discriminant analysis of radiometrically corrected remote sensing imagery. Int. J. Remote Sens. 32, 1983–2011.

Newton, A.C., Hill, R.A., Echeverría, C., Golicher, D., Rey Benayas, J.M., Cayuela, L., Hinsley, S.A., 2009. Remote sensing and the future of landscape ecology. Prog. Phys. Geogr. 33, 528–546.

Nuarsa, I.W., Nishio, F., Hongo, C., 2010. Development of the empirical model for rice field distribution mapping using multi-temporal Landsat ETM+ data: case study in Bali Indonesia. In: International Archives of the Photogrammetry, Remote Sensing and Spatial Information Science, XXXVIII, part 8, Kyoto Japan.

Oliveras, I., Gracia, M., Moré, G., Retana, J., 2009. Factors influencing the pattern of fire severities in a large wildfire under extreme meteorological conditions in the Mediterranean basin. IJWF 18, 755–764.

Pérez-Cabello, F., Ibarra, P., Echeverría, M.T., de la Riva, J., 2010. Post-fire land degradation of *Pinus sylvestris* L. woodlands after 14 years. Land Degrad. Dev. 21, 145–160.

Pesquer, L., Prat, E., Díaz-Delgado, R., Masó, J., Bustamante, J., Pons, X., 2012. Automatic modelling and continuous map generation from georeferenced species census data in an interoperable GIS environment. In: Proceedings of International Environmental Modelling and Software Society, ISBN: 978-88-9035-742-8.

Pesquer, L., Domingo, C., Pons, X., 2013a. A Geostatistical Approach for Selecting the Highest Quality MODIS Daily Images. Springer Lecture Notes in Computer Science Series, 7887 LNCS, pp. 608–615.

Pesquer, L., Pons, X., Cortés, A., Serral, I., 2013b. Spatial pattern alterations of JPEG2000 lossy compression in remote sensing images. Massive variogram analysis in High Performance Computing. J. Appl. Remote Sens., 73595.

Pons, X., Solé-Sugrañes, L., 1994. A simple radiometric correction model to improve automatic mapping of vegetation from multispectral satellite data. Remote Sens. Environ. 48, 191–204.

Pons, X., 2000. MiraMon. Geographical Information System and Remote Sensing Software, Centre for Ecological Research and Forestry Applications, CREAF, The Internet: http://www.creaf.uab.cat/MiraMon (accessed 02.01.14).

Pons, X., Arcalís, A., 2012. Diccionari terminològic de Teledetecció. Enciclopèdia Catalana and Institut Cartogràfic de Catalunya, Barcelona, ISBN: 978-84-412-2249-6.

Pons, X., Cristóbal, J., González, O., Riverola, A., Serra, P., Cea, C., Domingo, C., Díaz, P., Monterde, M., Velasco, E., 2012. Ten years of local water resource management: integrating satellite remote sensing and geographical information systems. Eur. J. Remote Sens. 45, 317–332.

Pons, X., Ninyerola, M., Cea, C., González-Guerrero, Ò., Serra, P., Zabala, A., Pesquer, L., Serral, I., Masó, J., Domingo, C., Serra, J.M., Cristóbal, J., Hain, C.R., Anderson, M.C., 2014. Preparing for global land cover & climate change mapping at detailed resolution. The design of a massive database from long time series of Landsat land cover products and in situ climate data. In: Global Vegetation Monitoring and Modeling symposium, GV2M. Avignon. Paper S2.16.

Potapov, P., Hansen, M.C., Stehman, S.V., Loveland, T.R., Pittman, K., 2008. Combining MODIS and Landsat imagery to estimate and map boreal forest cover loss. Remote Sens. Environ. 112, 3708–3719.

Proy, C., Tanrd, D., Deschamps, P.Y., 1989. Evaluation of topographic effects in remotely sensed data. Remote Sens. Environ. 30, 21–32.

Rabus, B., Eineder, M., Roth, A., Bamler, R., 2003. The shuttle radar topography mission – a new class of digital elevation models acquired by spaceborne radar. ISPRS J. Photogrammetry Remote Sens. 57, 241–262.

Riaño, D., Chuvieco, E., Salas, J., Aguado, I., 2003. Assessment of different topographic corrections in Landsat-TM data for mapping vegetation types. IEEE Trans. Geosci. Remote Sens. 41, 1056–1061.

Richards, J., Jia, X., 2005. Remote Sensing Digital Image Analysis: An Introduction, fourth ed. Springler-Verlag, Berlin.

Román-Cuesta, R.M., Retana, J., Gracia, M., Rodríguez, R., 2005. A quantitative comparison of methods for classifying burned areas with LISS-III imagery. Int. J. Remote Sens. 26, 1979–2003.

Roy, D., Borak, J., Devadiga, S., Wolfe, R., Zheng, M., Descloitres, J., 2002. The MODIS land product quality assessment approach. Remote Sens. Environ. 83, 62–76.

Sánchez, N., Martínez-Fernández, J., Calera, A., Torres, E., Pérez-Gutiérrez, C., 2010. Combining remote sensing and in situ soil moisture data for the application and validation of a distributed water balance model (HIDROMORE). Agric. Water Manage. 98, 69–78.

Schroeder, T.A., Cohen, W.B., Song, C., Canty, M.J., Yang, Z., 2006. Radiometric correction of multi-temporal Landsat data for characterization of early successional forest patterns in western Oregon. Remote Sens. Environ. 103, 16–26.

Serra, P., Pons, X., Saurí, D., 2003. Post-classification change detection with data from different sensors: some accuracy considerations. Int. J. Remote Sens. 24, 3311–3340.

Serra, P., Moré, G., Pons, X., 2009. Thematic accuracy consequences in cadaster land-cover enrichment from a pixel and from a polygon perspective. Photogram. Eng. Remote Sens. 75 (12), 1441–1449.

Slater, J.A., Heady, B., Kroenung, G., Curtis, W., Haase, J., Hoegemann, D., Shockley, C., Tracy, K., 2011. Global assessment of the new ASTER global digital elevation model. Photogram. Eng. Remote Sens. 77, 335–350.

Song, C., Woodcock, C.E., Seto, K.C., Lenney, M.P., Macomber, S.A., 2001. Classification and change detection using Landsat TM data when and how to correct atmospheric effects? Remote Sens. Environ. 75, 230–244.

Teillet, P.M., Guindon, B., Goodeonugh, D.G., 1982. On the slope-aspect correction of multispectral scanner data. Can. J. Remote Sens. 8, 84–106.

Themistocleous, K., Hadjimitsis, D.G., Retalis, A., Chrysoulakis, N., 2012. Development of a new image based atmospheric correction algorithm for aerosol optical thickness retrieval using the darkest pixel method. J. Appl. Remote Sens. 6, 063538.

U.S. Geological Survey, 2013. Product guide: Landsat climate data record (CDR). Surface reflectance. Department of the Interior U.S. Geological Survey. Version 3.4, December 2013, The Internet: http://landsat.usgs.gov/documents/cdr_sr_product_guide.pdf (accessed 02.01.14).

Vanonckelen, S., Lhermitte, S., Van Rompaey, A., 2013. The effect of atmospheric and topographic correction methods on land cover classification accuracy. Int. J. Appl. Earth Observ. Geoinform. 24, 9–21.

Vázquez, A., 2008. Structural attributes of three forest types in central Spain and Landsat ETM+ information evaluated with redundancy analysis. Int. J. Remote Sens. 29 (19), 5657–5676.

Veraverbeke, S., Verstraeten, W.W., Lhermitte, S., Goossens, R., 2010. Illumination effects on the differenced Normalized Burn Ratios optimality for assessing fire severity. Int. J. Appl. Earth Observ. Geoinform. 12, 60–70.

Vermote, E.F., Vogelmann, J., Wulder, M.A., Wynne, R., 2008. Free access to landsat imagery. Science 320 (5879), 1011.

Vermote, E.F., Kotchenova, S.Y., 2008. Atmospheric correction for the monitoring of land surfaces. J. Geophys. Res. 113 (D23), D23S90, http://dx.doi.org/10.1029/2007JD009662.

Vicente-Serrano, S.M., Pérez-Cabello, F., Lasanta, T., 2008. Assessment of radiometric correction techniques in analyzing vegetation variability and change using time series of Landsat images. Remote Sens. Environ. 112, 3916–3934.

Vincini, M., Reeder, D., 2000. Minnaert topographic normalization of Landsat TM imagery in rugged forest areas. Int. Arch. Photogram. Remote Sens. XXXIII (Part B7), Amsterdam.

Wallace, C.S.A., Watts, J.M., Yool, S.R., 2000. Characterizing the spatial structure of vegetation communities in the Mojave Desert using geostatistical techniques. Comput. Geosci. 26, 397–410.

Wilson, J.P., Gallant, J.C., 2000. Terrain Analysis. Principles and Applications. John Wiley & Sons, New York.

Yi, Y., Yang, D., Huang, J., Chen, D., 2008. Evaluation of MODIS surface reflectance products for wheat leaf area index (LAI) retrieval. ISPRS J. Photogram. Rem. Sens. 63, 661–677.

Zabala, A., Pons, X., 2002. Image Metadata: compiled proposal and implementation. In: Benes, T. (Ed.), Geoinformation for European-wide Integration. Millpress, Rotterdam, pp. 647–652, ISBN: 90-77017-71-2.

Zabala, A., Pons, X., 2011. Effects of lossy compression on remote sensing image classification of forest areas. Int. J. Appl. Earth Observ. Geoinform. 13, 43–51.

Zha, Y., Gao, J., Ni, S., Liu, Y., Jiang, J., Wei, Y., 2003. A spectral reflectance-based approach to quantification of grassland cover from Landsat TM imagery. Remote Sens. Environ. 87, 371–375.

Zha, Y., Gao, J., Nia, S., Shena, N., 2005. Temporal filtering of successive MODIS data in monitoring a locust outbreak. Int. J. Remote Sens. 26, 5665–5674.

Zhang, W., Gao, Y., 2011. Topographic correction algorithm for remotely sensed data accounting for indirect irradiance. Int. J. Remote Sens. 32 (7), 1807–1824.